High-resolution terahertz-driven atom probe tomography

Angela Vella[1,2]*, Jonathan Houard[1], Laurent Arnoldi[1], Mincheng Tang[1], Matthias Boudant[1], Anas Ayoub[1], Antoine Normand[1], Gerald Da Costa[1], Ammar Hideur[3]

Ultrafast control of matter by a strong electromagnetic field on the atomic scale is essential for future investigations and manipulations of ionization dynamics and excitation in solids. Coupling picosecond duration terahertz pulses to metallic nanostructures allows the generation of extremely localized and intense electric fields. Here, using single-cycle terahertz pulses, we demonstrate control over field ion emission from metallic nanotips. The terahertz near field is shown to induce an athermal ultrafast evaporation of surface atoms as ions on the subpicosecond time scale, with the tip acting as a field amplifier. The ultrafast terahertz-ion interaction offers unprecedented control over ultrashort free-ion pulses for imaging, analyzing, and manipulating matter at atomic scales. Here, we demonstrate terahertz atom probe microscopy as a new platform for microscopy with atomic spatial resolution and ultimate chemical resolution.

INTRODUCTION

Coupling electromagnetic fields to solid-state nanostructures to control the basic properties of matter at the nanoscale is attracting increasing interest for various applications such as chemistry and catalysis, nanopatterning or nanolithography, gas sensing, as well as ultrafast electron microscopy and imaging (*1*–*5*). In the context of matter analysis, field emission of positive ions from a sharp tip (also referred to as field evaporation) is the basic principle of atom probe tomography (APT), which is an imaging technique based on controlled field evaporation of atoms from a nanometric needle-shaped sample under a strong electric field (*6*). The attraction of APT lies in its capability to provide subnanometer spatial resolution in the three dimensions of space, with high chemical sensitivity across the whole periodic elements and their isotopes (*7*). Initially, APT was restricted to conductive materials because of the use of high-voltage pulses to trigger ion evaporation (*8*). The development of the laser-assisted APT (La-APT) (*9*) has enabled the APT analysis of semiconducting and dielectric materials (*10*). In La-APT, the sample is evaporated atom by atom by the combined actions of a high DC field and an ultrashort laser pulse (*11*, *12*). However, this La-APT usually suffers from low spatial and chemical resolutions due to the thermal heating arising from laser light absorption (*11*, *13*). Recent advances in electrons field emission show that ultrashort terahertz pulses (*14*) coupled to metallic nanostructures provide a unique route for the control (*15*–*20*) of electron dynamics at the nanoscale due to their large ponderomotive energy and low photon energy. The potential for terahertz-based APT to perform high-resolution imaging is thus very promising, but it is essential that we acquire a deeper understanding of the physics underlying terahertz-pulse-matter interaction within the APT operation environment.

Here, we show that the enhancement of terahertz fields in positively biased nanotips allows triggering the emission of positively charged ions from the nanostructure surface. On the basis of this effect, we demonstrate a high chemical and spatial resolution terahertz-assisted APT instrument.

[1]GPM UMR CNRS 6634, Normandie Université, Université-INSA de Rouen, Avenue de l'Université BP 12, 76801 Saint Etienne du Rouvray, France. [2]Institut Universitaire de France (IUF), France. [3]CORIA UMR CNRS 6614, Normandie Université, Université-INSA de Rouen, Avenue de l'Université BP 12, 76801 Saint Etienne du Rouvray, France.
*Corresponding author. Email: angela.vella@univ-rouen.fr

RESULTS

The experiment representing the Tera-APT microscope is sketched in Fig. 1A. A single-cycle strong terahertz field generated from two-color air plasma is focused on an aluminum tip biased at several kilovolts. A near-infrared (NIR) pulse (800-nm wavelength and 45-fs pulse duration) can be combined with the terahertz pulse and collinearly focused on the sample, with a variable time delay between the two pulses. The atoms at the surface of the aluminum tip are field-evaporated as ions by the combined action of the static field and the terahertz (or NIR) pulse that triggers the evaporation process. Ions are projected on a time- and position-sensitive detector (PSD). From the time-of-flight measurements, we retrieve the mass/charge ratio, and from the impact position on the detector system, we reconstruct the evaporated volume, using a reverse projection law (see Figs. 1D and movie S1) (*21*).

Near-terahertz field characterization and calibration

The temporal traces of the generated terahertz pulses are reported in Fig. 2B, for two inverted field directions (polarities) measured by electro-optic (EO) sampling outside the atom probe chamber. The terahertz field at the apex of the sample (near terahertz field) was measured using this field to drive electron emission from the negatively biased aluminum tip (*22*, *23*). First, we measured the electron emission properties of the aluminum tip (70-nm apex radius) under NIR illumination at I_{NIR} = 2.3 GW/cm^2 as a function of the negative bias, which shows that the tip acts as an ultrafast rectifying diode (Fig. 2A). Then, for the two incident terahertz transients of opposite polarities of Fig. 2B, we recorded the emission current as a function of the delay between the terahertz and the NIR laser pulses (Fig. 2C). Owing to the results of Fig. 2A, a correspondence between the bias (V_{DC}) and the emission current (flux) can be established and used to convert the measured flux of electrons into equivalent rectified potential (V_{THz}). We have thus reconstructed the rectified terahertz pulse at the nanotip apex, taking into account the fact that, changing the polarity from positive to negative, the terahertz field was

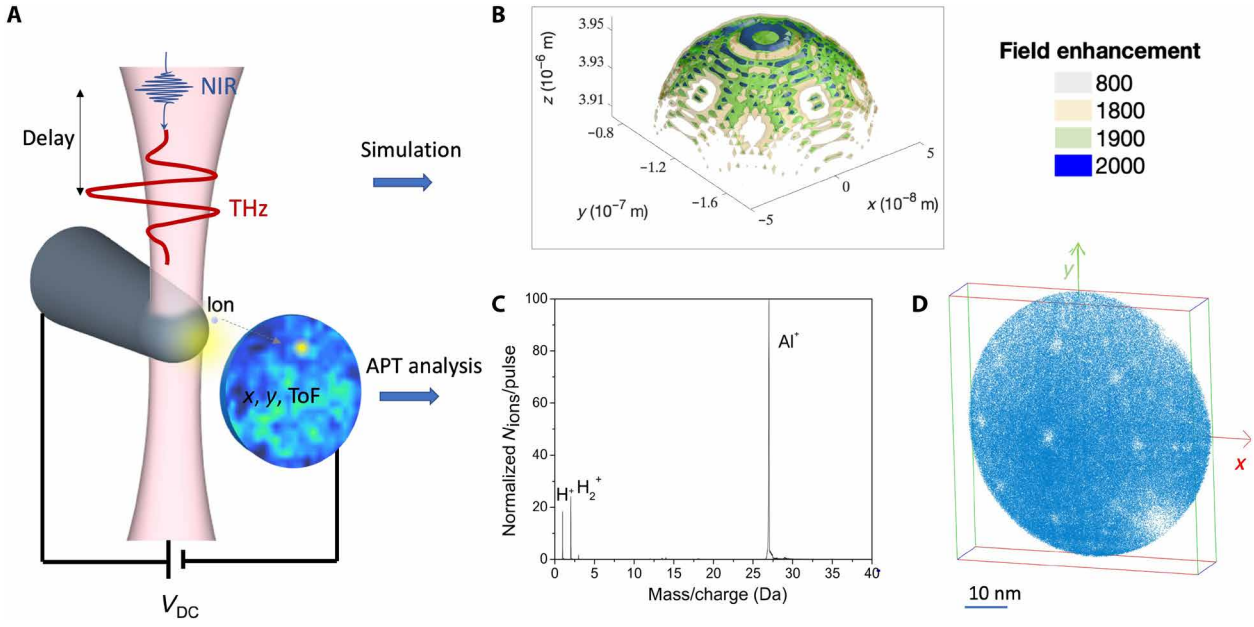

Fig. 1. Ion field evaporation triggered by terahertz in a tomographic atom probe. (**A**) Ultrashort terahertz (red) pulses are focused onto a metallic nanotip inside a high vacuum chamber. The high voltage applied to the metallic tip translates into an intense electric field at the specimen apex. The evaporated ions are projected toward a time-sensitive detector and a PSD located at 10 cm from the nanotip. A NIR pulse (blue) can be combined to the terahertz pulse with a variable delay to probe the interaction mechanisms. ToF, time of flight. (**B**) Isosurface plots of the three-dimensional (3D) field distributions calculated numerically for the excitation frequency of 2 THz and for different values of the field enhancement factor. (**C**) Mass spectrum as measured from a terahertz-assisted atom probe analysis of a pure aluminum specimen. The datasets consist of around 10^5 ions collected at a bias voltage V_{DC} = 8.7 kV and an evaporation rate of 0.01 ion per pulse at T = 50 K. (**D**) 3D reconstruction of a pure aluminum specimen.

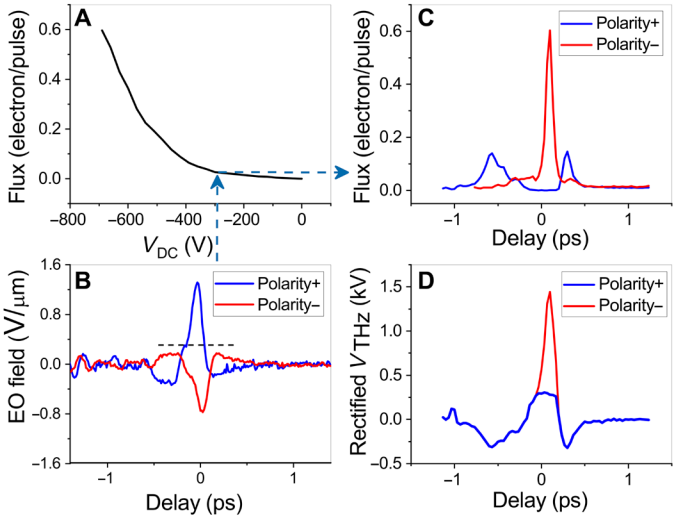

Fig. 2. Rectified terahertz voltage at the tip apex. (**A**) Current-voltage characteristic of electron emission obtained from an aluminum tip (apex radius of 70 nm) under laser illumination at I_{NIR} = 2.3 GW/cm^2. (**B**) Two terahertz transients with inverted field directions (polarity) measured by EO sampling outside the atom probe chamber. (**C**) Photocurrent modulation for the terahertz waveforms corresponding to the EO traces of (B) at V_{DC} = −300 V and I_{NIR} = 2.3 GW/cm^2. (**D**) Rectified terahertz pulse reconstructed from (A) and (C).

attenuated of a factor 2 (see Fig. 2D). We observed same deviation from the incident terahertz pulse, due to the antenna response of the tip (*23*, *24*).

We converted the measured rectified terahertz voltage into the near field using the relation $F^0_{THz} = V_{THz}/(kR)$, with k as a geometrical factor ranging from 4 to 9 and R as the apex radius. To measure the k factor, we field-evaporated the sample biased to 9 kV using only NIR laser pulses of I_{NIR} = 2.3 GW/cm^2. Following the Kingham theory (*25*), from the ratio of the Al^+/Al^{2+} peaks in the collected spectrum reported in Fig. 3A, we calculated the surface field at 17 V/nm leading to a geometric factor value of k = 7.6. The amplitude of the terahertz pulse in Fig. 2D is therefore 2.72 V/nm, about 2000 times higher than the incident terahertz field of Fig. 2B.

We computed the field enhancement factor by solving Maxwell equations in three dimensions using a finite-difference time domain commercial software (Lumerical), allowing to take into account the tip geometry (*26*). In this simulation, the tip is modeled as a cone terminated by a hemispheric cap (see Fig. 1B). It is placed in the simulated space and surrounded by a perfectly matched layer avoiding any field reflection. For 2 THz, corresponding to the central frequency of incident terahertz signal of Fig. 2D, the material properties are taken into account through the dielectric constant considering the value given in (*27*). In Fig. 1B four field isosurfaces are represented, corresponding to field enhancement factor values ranging from 800 to 2000. For the field enhancement value of 2000, the isosurface corresponds to the surface of the simulated volume. Because the field enhancement is highly frequency dependent with a typical 1/frequency behavior (*23*) and because the excitation spectrum of the incident terahertz pulse centered at 2 THz has a full width at half maximum of about 1 THz, the value of the field enhancement will range between 4000 and 1300. The experimental value of 2000 can be considered as the mean value of the enhancement factor on the range of the excitation frequencies.

To perform ion field emission using terahertz pulses, we increased the amplitude of the terahertz field to its maximum of 5.5 V/μm.

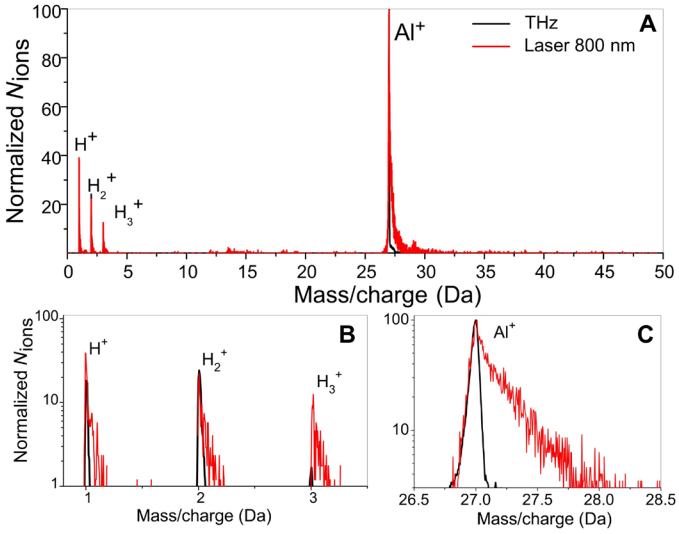

Fig. 3. Analyzing aluminum nanotip in terahertz-assisted APT. (**A**) Mass spectra as measured from a terahertz-assisted atom probe analysis (black) and a NIR laser–assisted atom probe analysis (red) of a pure aluminum specimen. The datasets consist of around 10^5 ions collected at a bias voltage $U_{bias} = 9$ kV, NIR laser intensity $I_{NIR} = 2.3$ GW/cm^2, and an evaporation rate of 0.01 ion per pulse at $T = 50$ K. (**B**) Zoom on H^+, H_2^+, and H_3^+ mass peaks using semilog scale. (**C**) Zoom on Al^+ mass peak using semilog scale.

Taking into account the value of the enhancement factor (2000), the amplitude of the terahertz near field was about 10.5 V/nm. We experimentally checked this value of the terahertz near field by electron energy filtering. The maximum terahertz field, with negative polarity, was focused on the sample biased at the positive voltage of about 3 kV. The bias voltage was then slowly decreased, and no electron emission was detected up to a bias of 1.4 kV. Because electrons escape the enhanced near terahertz field within a small fraction of the oscillation period, the corresponding yielding electron energy is $E_{THz} = e \int F_{THz}(r, t_0)dr$, where t_0 is the time of emission (*17*). We describe the terahertz by its field strength at the tip apex surface F^0_{THz} and a dipolar spatial decay of length R, equal to the tip radius. It follows that $E_{THz} = 2e F^0_{THz} R$. The electron energy loss due to the positive bias is $E_{DC} = eV_{DC}$. The energy of the electrons detected at $V_{DC} = 1.4$ kV is almost equal to zero; therefore, $E_{THz} = E_{DC}$ and the terahertz field strength at the tip apex surface is $F^0_{Thz} = \frac{eV_{DC}}{2eR} = 10$ V/nm, in good agreement with the value calculated using the enhancement factor of 2000.

Analyzing aluminum nanotip in terahertz-assisted APT

To perform ion field evaporation by terahertz pulses, we positively biased the aluminum tip (70-nm apex radius) at 9 kV and set the terahertz pulse with positive polarity (Fig. 2B) to its maximum amplitude of 5.5 V/μm, which corresponds to a near field of 10.5 V/nm. In Fig. 3A, we have presented the mass spectra obtained at the same bias using terahertz and NIR laser pulses. Same species are detected from both spectra; however, the width of the peaks [Δ(*mass*/*charge*) at 50, 10, or 1% of the maximum peak height] is much larger when NIR pulses are used, as shown in Fig. 3, B and C. The mass/charge resolving power and thus the chemical resolution of the atom probe are related to the width of peaks identified on the mass spectrum through the relation (*mass*/*charge*)/Δ(*mass*/*charge*) (*11*). For the Al^+ peak, the mass resolving powers of 380, 180, and 60 are obtained at 50, 10, and 1% of the maximum peak height, respectively. These values at 10 and 1% are four times larger than those obtained using NIR pulses.

The spatial distribution of the Al^+ ions on the detector is reported in Fig. 4A. When the sample is crystalline, such as aluminum, the

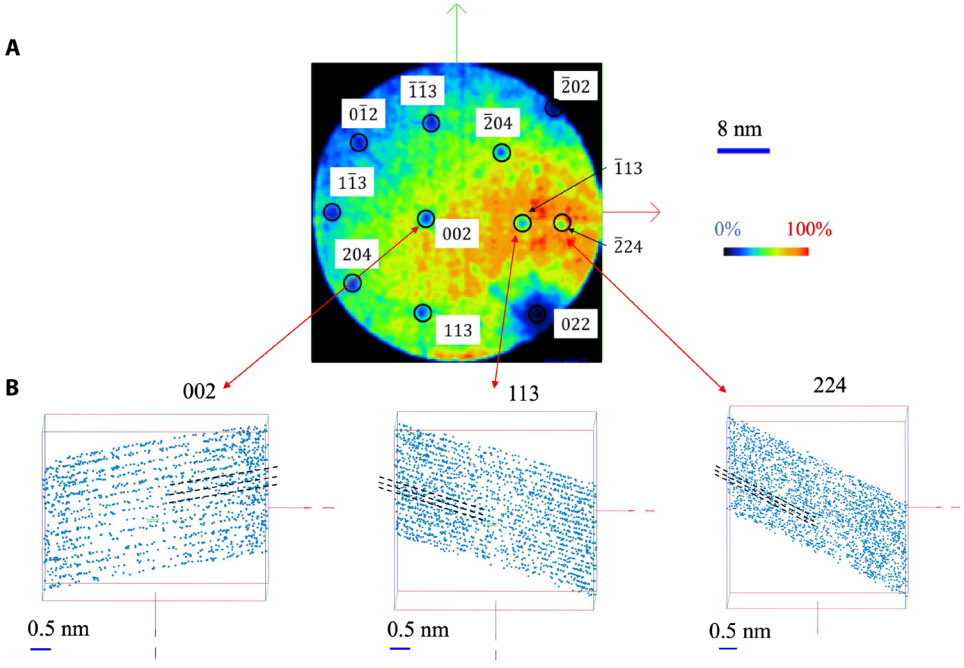

Fig. 4. Analyzing aluminum nanotip in terahertz-assisted APT. (**A**) Spatial distribution of Al^+ ions on the detector for the terahertz-assisted atom probe analysis. (**B**) 3D images resulting from the terahertz-assisted atom probe analysis showing Al atomic planes along the <002>, <113>, and < 224> crystallographic directions; black dotted lines are guides to the eye.

regular crystal structure is intercepted by the hemispherical shape of the tip, and it creates regular structures of concentric atomic rings known as poles. The rings are visible on the evaporation (movie S1). The center of the <*hkl*> pole is the position where the atomic planes (*hkl*) are tangent to the hemispherical surface. At the center of the pole, the local field is lower than on its border; therefore, the number of the evaporated atoms will be lower at the center. It follows that poles can be associated with the regions of lower number of impacts on the map in Fig. 4A. The three-dimensional (3D) reconstruction of the evaporated volume shows well-resolved atomic planes for three crystallographic directions, as shown in Fig. 4B, which are indiscernible in the case of NIR analysis (for more details about the atomic spacing measurement, see the Supplementary Materials). Because the image reconstruction in APT is obtained by field erosion, which governs the in-depth (longitudinal) dimension, and the ion projection, which gives rise to the lateral dimensions, the longitudinal resolution of the image is different from its lateral one. The two values of the spatial resolution of the 3D images of Fig. 4B were calculated using the Fourier transform approach (*28*, *29*). The measured longitudinal and lateral resolutions are (0.07 ± 0.01) nm and (1.3 ± 0.1) nm, respectively. The in-depth resolution is limited by the perturbation of the well-ordered sequence of the evaporation of atoms from the surface. The lateral resolution is mainly limited by surface diffusion before field evaporation (trajectory aberrations in the first steps of flight, for example).

Dual-frequency excitation of the aluminum nanotip

Using dual-frequency excitation of the aluminum nanotip, we have recorded the evaporation rate as a function of the delay between the terahertz and the NIR laser pulses (Fig. 5C). For large negative delay (< − 1 ps) that is a situation in which the terahertz pulse precedes the NIR pulse, the evaporation rate is stable and its value is equal to that obtained only by terahertz pulses; therefore, it is unaffected by the NIR laser excitation. For negative delays in the range of temporal overlap between the NIR and the terahertz pulse (−1 < delay < 0 ps), the evaporation rate remains unchanged. When the delay becomes positive and the NIR pulse precedes the terahertz pulse, the evaporation rate increases up to its maximum in less than 0.5 ps. For longer positive delay, it stays stable to its maximum value. Because the evaporation rate is a function of the lattice temperature by this dual-frequency excitation, we are following NIR laser heating in the nanotip apex via terahertz field emission, as will be discussed in the next section.

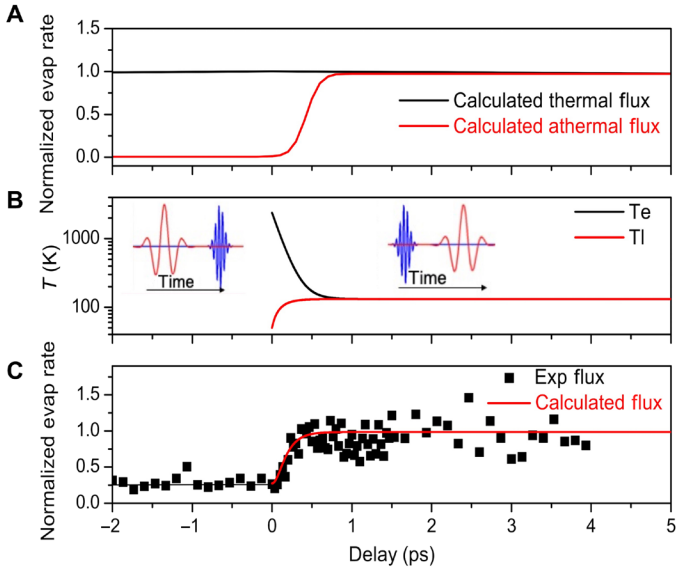

Fig. 5. Following NIR laser heating in the nanotip apex via terahertz field emission. (**A**) Normalized evaporation rate calculated considering a thermal (black) or athermal (red) evaporation mechanism for the terahertz pulse and a thermal mechanism for the NIR laser pulse as a function of the delay between these two pulses as sketched in Fig. 1A. (**B**) Electronic and lattice temperatures computed in a two-temperature model for parameters of the measurement in (C). (**C**) Transient terahertz field evaporation (black squares) as a function of the delay between the NIR and the terahertz pulses. The datasets consist of around 10^3 ions per step collected at V_{DC} = 8.9 kV, NIR laser intensity I_{NIR} = 0.5 GW/cm^2, and an evaporation rate of 0.01 ion per pulse using only terahertz pulses and 0.001 ion per pulse using only NIR laser pulses, at T = 50 K.

DISCUSSION

Ion trajectory calculation

The improvement in the chemical and spatial resolution of the atom probe assisted by terahertz pulses compared to NIR pulses is due to the change in the underlying physical evaporation mechanism. In the case of NIR illumination, the field ion evaporation is triggered by intermediate thermal pulses generated by the NIR laser–sample interaction (*30*). The typical duration of this thermal pulse is of hundreds of picoseconds in the case of aluminum (*31*). This long thermal pulse is at the origin of the evaporation of ions long after the arrival of the laser pulse. This effect is visible in the time-of-flight spectrum of Al^+ ions, which exhibits an exponential decay curve with about 2.5-ns decay time, in Fig. 6B. For terahertz illumination, the time-of-flight Al^+ peak shows also an asymmetrical shape, compared to the Gaussian profile represented in green in Fig. 6B. However, in this case, decay time is very short compared to NIR illumination. Numerical modeling of the time-of-flight spectrum allows for a comprehensive description of the ion flight to the detector. We have calculated the Al^+ ion trajectories taking into account both the locally enhanced terahertz and the constant electric field to compute the ion trajectories for different evaporation times t_0 (departure time) relative to the terahertz pulse (*32*). For simplicity, we consider a 1D propagation. We model the static field as a superposition of a homogeneous long range component and a more confined component with a near-field dipole decay length equal to the tip apex-radius R (*32*)

$$F_{stat}(x) = F^0_{stat}\frac{d^3}{(d+x)^3} + F_{hom}$$

with F^0 = 15.75 V/nm, F_{hom} = 6.93 × 10^{-5} V/nm, and $d = \frac{R}{\sqrt[3]{2}-1}$ a rescaled parameter. The variables for the static electric field are constrained to satisfy the total energy eV_{DC} gained by the bias voltage.

The terahertz transient is reported in Fig. 6A, as function of time. Its spatial dependence follows the near-field dipole decay (*24*)

$$F_{Thz}(x,t) = F_{Thz}(t)\frac{d^3}{(d+x)^3}$$

where the maximum of the function $F_{Thz}(t)$ is F^0_{Thz} = 10.5 V/nm. Ion trajectories are calculated solving the differential equation

$$m\ddot{x} = ne(F_{stat}(x) + F_{Thz}(x, t+t_0)) \quad (1)$$

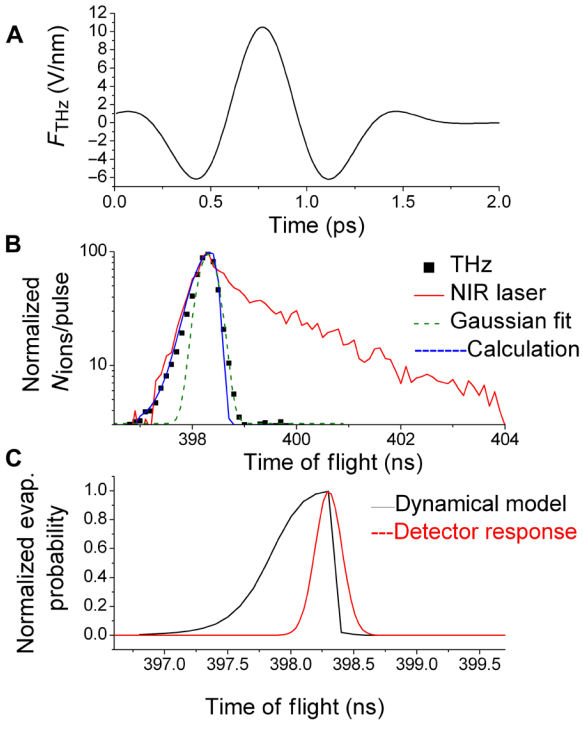

Fig. 6. Experimental measurement and numerical simulation of the spectral shape of the terahertz-assisted APT. (**A**) Terahertz transient used for the calculation of ion trajectories. (**B**) Al^+ time-of-flight peak as measured from a terahertz-assisted atom probe analysis (black squares) and a NIR laser–assisted atom probe analysis (red line) of a pure aluminum specimen. Best fit of the terahertz Al^+ time-of-flight peak using a Gaussian function (dashed green line) underlines the asymmetry of the Al^+ peak for both the terahertz and NIR laser–assisted atom probe analyses. The calculated shape of the Al^+ time-of-flight peak (blue line), solving the ion propagation equation under the combined actions of the terahertz and static fields. The experimental conditions are the same as those of Fig. 2. (**C**) Normalized evaporation probability (black) calculated for ions emitted at different times t_0 relative to the terahertz pulse as a function of the associated time of flight. The detector response function (red) corresponding to a Gaussian function of 150 ps in width.

where m is the mass and ne is the charge. The initial conditions are $x(0) = 0$ and $\dot{x}(0) = 0$.

For each t_0, we have calculated the time of flight and the evaporation probability ϕ. For electric fields close to the evaporation field threshold of the material, the evaporation probability (or rate) is given by $\phi_2 \propto \exp\left(-\frac{Q(F)}{k_B T}\right)$, where the activation energy $Q(F) = Q_0\left(\frac{F_{evap}}{F} - 1\right)$ with $Q_0 = 0.04$ eV, $F_{evap} = 20$ V/nm, k_B is the Boltzmann constant, and T is the lattice temperature. For electric fields higher than the value of the evaporation field, the evaporation probability was set to 1 (*12*). We represent the normalized evaporation probability of ions emitted at t_0 as a function of the associated time of flight in Fig. 6C. Because of their large mass, compared to electrons, Al^+ ions cannot escape the enhanced terahertz field within a fraction of the terahertz oscillation period, resulting in the ion momentum governed by the temporal integral over the total field along the individual trajectories $x(t)$: $P = e\int_{t_0}^{\infty} F(t, x(t))\,dt$. Because trajectories depend on the emission time (see the Supplementary Materials), the momentum is different from the temporal integral of the terahertz field. We also convolute the evaporation probability with the response function of the detector, a Gaussian of 150 ps in width (*33*). This simple model reproduces quite well the experimental shape of the Al^+ spectral peak (Fig. 6B). Concerning the hydrogen peaks (H^+ and H_2^+), a larger dispersion is calculated because of their lower mass compared to Al^+ ions. However, because of the low number of detected hydrogen ions, these predictions cannot be confirmed by the experimental measurements.

Determination of the evaporation mechanism

The results of the dual-frequency excitation of the aluminum nanotip constitute the experimental proof of the athermal ion evaporation by terahertz pulses. We know that the evaporation rate is a function of the lattice temperature and of the activation energy that decreases when the surface field increases. Moreover, we know that the NIR pulse acts on the evaporation rate increasing the lattice temperature in a time scale of less than 1 ps (*31*). Instead, we suppose that the terahertz pulse acts only on the surface field by reducing the activation barrier (*34*). Therefore, if the NIR laser pulse illuminates the sample at $t = 0$ s, then the sample temperature will increase as follows

$$T(t) = T_0 + \frac{T_{rise}}{2}\left(1 - erf\left(\frac{t - t_0}{t_c}\right)\right) \quad (2)$$

with $T_0 = 50$ K, $T_{rise} = 60$ K, $t_0 = 0.3$ ps, and $t_c = 0.25$ ps, corresponding to the electron-phonon coupling time. The temporal shape of the terahertz pulse close to its maximum can be approximated by the Gaussian function

$$Fg_{THz}(t) = F^0_{THz}\exp\left(-\left(\frac{t - t_{max}}{0.5}\right)^2\right)$$

where $t_{max} = 0.77$ ps corresponds to the time position of the terahertz pulse peak of Fig. 6A. Because the activation barrier decreases proportionally to the electric field strength, we assume that, when the terahertz pulse is almost at its maximum value, the barrier evolves following the Gaussian shape of the terahertz pulse, as follows

$$Qg(t) = Q_{DC} - \Delta Q\exp\left(-\left(\frac{t - t_{max}}{0.5}\right)^2\right)$$

with $Q_{DC} = 0.11$ eV and $\Delta Q = 0.7$ eV. The value of ΔQ was fixed considering that close to the maximum of the terahertz pulse, the barrier is of 0.04 eV. The value of Q_{DC} was estimated from the experimental value of the detected flux under only NIR illumination. The evaporation rate follows a Boltzmann law as a function of the sample temperature and the activation barrier: $\phi \propto \exp(-Q/k_B T)$.

Therefore, integrating on the acquisition time, the evaporation rate as a function of the delay τ between the terahertz and NIR pulses becomes

$$\phi(\tau) \propto \int_0^{\infty} \exp\left(-\frac{Qg(t)}{k_B T(t + \tau)}\right)dt \quad (3)$$

We represent the evolution of ϕ as function of the delay in Fig. 5A (labeled "calculated athermal flux"), and it well describes the experimental behavior of Fig. 5C. On the contrary, if we assume that the terahertz pulse acts as a thermal pulse and we use Eq. 2 to model the temperature evolution after the terahertz illumination, then the evolution of ϕ as a function of the delay is constant on the range of delays explored experimentally, as shown in Fig. 5A, with black curve labeled

"calculated thermal flux." Therefore, this curve does not reproduce the experimental behavior of Fig. 5C. We can conclude that the assumption of a terahertz-induced thermal pulse is false (more details on the calculation are in the Supplementary Materials).

The temporal increase in the evaporation rate at positive delays of Fig. 5C measures the heating of the lattice due to the relaxation of the electronic temperature after the NIR laser excitation (*31*). To describe this heating process, we have regarded electron-phonon coupling as the exclusive cooling channel in the first few picoseconds following the electron excitation. We have modeled this behavior by calculating the electronic (T_e) and lattice (T_l) temperatures in a two-temperature model (*35*) (Fig. 5B). We have used the experimental excitation parameters and the material constants for bulk aluminum but, because of the nanoscale carrier confinement, not ballistic or diffusive spatial energy transport. The electron-phonon coupling constant of bulk is expected to be unaffected by the nanoscopic geometry (*36*). The temporal evolution of the electronic and lattice temperature is represented in Fig. 5B. We note that, 1 ps after the NIR excitation, the two thermodynamic systems (electrons and lattice) are at the equilibrium at 130 K.

For the calculated values of the lattice temperature (T_l), we evaluate the terahertz-induced evaporation rate ($\phi \propto \exp(-Q/k_B T_l)$) for the activation energy barrier of $Q = 0.04$ eV (*12*). This calculated flux is reported in Fig. 5C. This simplified model accurately reproduces the experimental increase in the evaporation rate at positive delay (Fig. 5C).

In conclusion, we demonstrate ultrafast, nonthermal field evaporation of surface atoms as ions by tip-enhanced single-cycle terahertz pulses. Essentially, the results represent the implementation of an ultrafast field–assisted atom probe triggered by terahertz pulses, thus paving the path for material analysis with ultimate spatial and chemical resolutions. The approach has notable potential for atom probe analysis of biological materials where thermal heating constitutes a strong limitation. The field evaporation assisted by terahertz pulses will also enable time-resolved chemistry in high electric field, opening the way for new degrees of freedom in the control of field-induced chemistry. The narrow energy spread of the field-evaporated ions by single-cycle terahertz pulses opens the way to their use as charged particle beams to image, analyze, and modify matter from the microscale to the nanoscale.

MATERIALS AND METHODS

Laser-assisted APT

Experiments were performed inside a home-made ultrahigh-vacuum atom probe chamber with a base pressure of 5×10^{-10} mbar and a close loop cryostat cooling of the sample to 50 K. The aluminum tip was electrochemically etched from a 0.25-mm-diameter aluminum wire. The tip was cleaned inside the chamber using NIR laser evaporation. The tip is polarized with a positive applied DC bias V_{DC}, yielding an intense field at the tip apex. Field ion evaporation is triggered by a femtosecond NIR laser pulse (800 nm in wavelength) with tunable energy up to 3.5 μJ. Surface atoms may ionize and leave the surface, flying toward a detector sensitive to the impact position of the ion and to its time of flight. The time of flight of the ions allows for the identification of their mass/charge ratio, i.e., (with some limitations) of their chemical identity. Furthermore, the impact position on the detector makes it possible to reconstruct the original position of each ion on the tip through a back-projection algorithm. It becomes thus possible to retrieve multidimensional information, such as 2D surface maps of emitted species or the 3D reconstruction of the chemical composition of a given volume.

The PSD used in this study is a delay line detector with improved multihit capabilities. It consists of a conventional 8-cm Roentdek delay line detector following a pair of microchannel plates (MCPs) in chevron configuration. Signal output from each end of the two wire pairs are digitized by means of fast digitizer boards PXI DC 271 (or Keysight U1051A Acqiris). Ion flight time signals are taken as output from the MCP, and the positioning is calculated using signals provided by the delay line outputs. A deconvolution algorithm is used to improve the multihit capabilities of the PSD. The 3D reconstruction of the evaporated volume has been obtained by applying the cone angle/initial tip radius protocol (*21*).

Ultrafast laser source and terahertz optics

The laser system is a Spitfire model from Spectra Physics delivering a 45-fs pulse in the infrared at 800-nm wavelength with a repetition rate of 1 kHz and a maximum energy of 4 mJ. It consists of a passively mode-locked titanium-sapphire (Ti:Sa) oscillator delivering sub–45-fs pulses at a 80-MHz repetition rate. The pulses from the oscillator are down-picked to a 1-KHz repetition rate and amplified in a chirped-pulse Ti:Sa amplifier chain. The output beam is a TEM00 Gaussian beam with a diameter of 8 mm. The beam is split in two parts (90/10 in energy); the highest-energy beam is used for terahertz generation, and it is mechanically chopped at 145 Hz. The low-energy beam is used either as probe for the temporal characterization of the terahertz pulses in an EO sampling setup based on a GaP crystal or as trigger for ion emission in a NIR laser–assisted atom probe. The terahertz pulse is generated by a two-color plasma generation process (*37*). The NIR laser beam is focused in air by a 40-cm focal lens and passes through a beta barium borate (BBO) crystal placed before the focal plane, to generate the second harmonic wave (SHW) at 400 nm. The focused bichromatic femtosecond laser pulses consisting of the fundamental wave (FW) at 800-nm wavelength and its SHW generate a plasma filament, which emits terahertz radiation with very high field strengths. The amplitude and polarity of the emitted terahertz pulses can be controlled by rotating the BBO crystal around its optical axis. The terahertz signal is collimated by a gold-coated parabolic mirror, and the residual FW and SHW components are filtered by a silicon window. The terahertz radiation can be alternatively focused on the EO system or on the nanotip inside the atom probe chamber. The EO detection system is composed by a 100-μm-thick GaP crystal, a Wollaston prism, and two balanced photodiodes connected to a lock-in amplifier (7265 Dual Phase from Ametek). The pulse polarity is controlled by acting on the phase difference between the NIR wave and its SHW as reported in (*17*).

For field emission analysis, the terahertz beam is sent into the analysis chamber through a transparent window, having a transmission of 70% in the low-terahertz frequency range between 0.1 and 10 THz. The beam is focalized on the biased nanotip by a spherical mirror placed inside the vacuum chamber. The actual beam spot size onto the specimen cannot be measured. It is estimated from simplified Gaussian beam propagation formula assuming focalization through a thin lens. The estimated beam waist values are 30 μm and 6 mm for the NIR and terahertz beams, respectively.

SUPPLEMENTARY MATERIALS

Supplementary material for this article is available at http://advances.sciencemag.org/cgi/content/full/7/7/eabd7259/DC1

REFERENCES AND NOTES

1. R. B. Sadeghian, M. S. Islam, Ultralow-voltage field-ionization discharge on whiskered silicon nanowires for gas-sensing applications. *Nat. Mater.* **10**, 135–140 (2011).
2. J.-F. Liu, G. P. Miller, Field-assisted nanopatterning. *J. Phys. Chem. C* **111**, 10758–10760 (2007).
3. A. V. Ovchinnikov, O. V. Chefonov, E. D. Mishina, M. B. Agranat, Second harmonic generation in the bulk of silicon induced by an electric field of a high power terahertz pulse. *Sci. Rep.* **9**, 9753 (2019).
4. P. Klarskov, H. Kim, V. L. Colvin, D. M. Mittleman, Nanoscale laser terahertz emission microscopy. *ACS Photonics* **4**, 2676–2680 (2017).
5. P. Dombi, Z. Pápa, J. Vogelsang, S. V. Yalunin, M. Sivis, G. Herink, S. Schäfer, P. Groß, C. Ropers, C. Lienau, Strong-field nano-optics. *Rev. Mod. Phys.* **92**, 025003 (2020).
6. D. Blavette, A. Bostel, J. M. Sarrau, B. Deconihout, A. Menand, An atom probe for three-dimensional tomography. *Nature* **363**, 432–435 (1993).
7. Y.-S. Chen, H. Lu, J. Liang, A. Rosenthal, H. Liu, G. Sneddon, I. McCarroll, Z. Zhao, W. Li, A. Guo, J. M. Cairney, Observation of hydrogen trapping at dislocations, grain boundaries, and precipitates. *Science* **367**, 171–175 (2020).
8. D. Blavette, E. Cadel, A. Fraczkiewicz, A. Menand, Three-dimensional atomic-scale imaging of impurity segregation to line defects. *Science* **286**, 2317–2319 (1999).
9. B. Gault, F. Vurpillot, A. Vella, M. Gilbert, A. Menand, D. Blavette, B. Deconihout, Design of a femtosecond laser assisted tomographic atom probe. *Rev. Sci. Instrum.* **77**, 043705 (2006).
10. K. Thompson, P. L. Flaitz, P. Ronsheim, D. J. Larson, T. F. Kelly, Imaging of arsenic Cottrell atmospheres around silicon defects by three-dimensional atom probe tomography. *Science* **317**, 1370–1374 (2007).
11. W. Lefebvre-Ulrikson, F. Vurpillot, X. Sauvage, *Atom Probe Tomography* (Academic Press, 2016).
12. M. Miller, R. Forbes, *Atom–probe Tomography: The Local Electrode Atom Probe* (Springer, 2014).
13. L. Mancini, N. Amirifar, D. Shinde, I. Blum, M. Gilbert, A. Vella, F. Vurpillot, W. Lefebvre, R. Lardé, E. Talbot, P. Pareige, X. Portier, A. Ziani, C. Davesnne, C. Durand, J. Eymery, R. Butté, J.-F. Carlin, N. Grandjean, L. Rigutti, Composition of wide bandgap semiconductor materials and nanostructures measured by atom probe tomography and its dependence on the surface electric field. *J. Phys. Chem. C* **118**, 24136–24151 (2014).
14. M. Sato, T. Higuchi, N. Kanda, K. Konishi, K. Yoshioka, T. Suzuki, K. Misawa, M. Kuwata-Gonokami, Terahertz polarization pulse shaping with arbitrary field control. *Nat. Photonics* **7**, 724–731 (2013).
15. J. Déchard, A. Debayle, X. Davoine, L. Gremillet, L. Bergé, Terahertz pulse generation in underdense relativistic plasmas: From photoionization-induced radiation to coherent transition radiation. *Phys. Rev. Lett.* **120**, 144801 (2018).
16. A. D. Koulouklidis, C. Gollner, V. Shumakova, V. Y. Fedorov, A. Pugžlys, A. Baltuška, S. Tzortzakis, Observation of extremely efficient terahertz generation from mid-infrared two-color laser filaments. *Nat. Commun.* **11**, 292 (2020).
17. L. Wimmer, G. Herink, D. R. Solli, S. V. Yalunin, K. E. Echternkamp, C. Ropers, Terahertz control of nanotip photoemission. *Nat. Phys.* **10**, 432–436 (2014).
18. S. Li, R. R. Jones, High-energy electron emission from metallic nano-tips driven by intense single-cycle terahertz pulses. *Nat. Commun.* **7**, 13405 (2016).
19. K. Yoshioka, I. Katayama, Y. Minami, M. Kitajima, S. Yoshida, H. Shigekawa, J. Takeda, Real-space coherent manipulation of electrons in a single tunnel junction by single-cycle terahertz electric fields. *Nat. Photonics* **10**, 762–765 (2016).
20. V. Jelic, K. Iwaszczuk, P. H. Nguyen, C. Rathje, G. J. Hornig, H. M. Sharum, J. R. Hoffman, M. R. Freeman, F. A. Hegmann, Ultrafast terahertz control of extreme tunnel currents through single atoms on a silicon surface. *Nat. Phys.* **13**, 591–598 (2017).
21. F. Vurpillot, B. Gault, B. P. Geiser, D. J. Larson, Reconstructing atom probe data: A review. *Ultramicroscopy* **132**, 19–30 (2013).
22. S. Yoshida, H. Hirori, T. Tachizaki, K. Yoshioka, Y. Arashida, Z.-H. Wang, Y. Sanari, O. Takeuchi, Y. Kanemitsu, H. Shigekawa, Subcycle transient scanning tunneling spectroscopy with visualization of enhanced terahertz near field. *ACS Photonics* **6**, 1356–1364 (2019).
23. J. Houard, L. Arnoldi, A. Ayoub, A. Hideur, A. Vella, Nanotip response to monocycle terahertz pulses. *Appl. Phys. Lett.* **117**, 151105 (2020).
24. K. Wang, D. M. Mittleman, N. C. J. Van der Valk, P. C. M. Planken, Antenna effects in terahertz apertureless near-field optical microscopy. *Appl. Phys. Lett.* **85**, 2715–2717 (2004).
25. D. R. Kingham, The post-ionization of field evaporated ions: A theoretical explanation of multiple charge states. *Surf. Sci.* **116**, 273–301 (1982).
26. L. Solutions, *Computer Software.* Vers. 8 (2017).
27. E. D. Palik, *Handbook of Optical Constants of Solids* (Academic Press, 1998), vol. 3.
28. F. Vurpillot, G. Da Costa, A. Menand, D. Blavette, Structural analyses in three-dimensional atom probe: A Fourier transform approach. *J. Microsc.* **203**, 295–302 (2001).
29. F. Vurpillot, L. Renaud, D. Blavette, A new step towards the lattice reconstruction in 3DAP. *Ultramicroscopy* **95**, 223–229 (2003).
30. A. Vella, On the interaction of an ultra-fast laser with a nanometric tip by laser assisted atom probe tomography: A review. *Ultramicroscopy* **132**, 5–18 (2013).
31. J. Houard, A. Vella, F. Vurpillot, B. Deconihout, Three-dimensional thermal response of a metal subwavelength tip under femtosecond laser illumination. *Phys. Rev. B* **84**, 033405 (2011).
32. L. Wimmer, O. Karnbach, G. Herink, C. Ropers, Phase space manipulation of free-electron pulses from metal nanotips using combined terahertz near fields and external biasing. *Phys. Rev. B* **95**, 165416 (2017).
33. G. Da Costa, H. Wang, S. Duguay, A. Bostel, D. Blavette, B. Deconihout, Advance in multi-hit detection and quantization in atom probe tomography. *Rev. Sci. Instrum.* **83**, 123709 (2012).
34. A. Vella, B. Deconihout, L. Marrucci, E. Santamato, Femtosecond field ion emission by surface optical rectification. *Phys. Rev. Lett.* **99**, 046103 (2007).
35. G. Herink, L. Wimmer, C. Ropers, Field emission at terahertz frequencies: AC-tunneling and ultrafast carrier dynamics. *New J. Phys.* **16**, 123005 (2014).
36. J. H. Hodak, A. Henglein, G. V. Hartland, Photophysics of nanometer sized metal particles: Electron−phonon coupling and coherent excitation of breathing vibrational modes. *J. Phys. Chem. B* **104**, 9954–9965 (2000).
37. T. Bartel, P. Gaal, K. Reimann, M. Woerner, T. Elsaesser, Generation of single-cycle THz transients with high electric-field amplitudes. *Opt. Lett.* **30**, 2805–2807 (2005).

Acknowledgments: We acknowledge F. Delaroche and C. Vaudolon for help for the development of the acquisition software and for the mechanical design. **Funding:** This work was supported by the French Agence Nationale de la Recherche (ANR), through the program "Investissements d'Avenir"(ANR-10-LABX-09-01), LabEx EMC3, Efesto project; by the European Union with the European Regional Development Fund (ERDF) and the Regional Council of Normandie; and by the Institut Carnot ESP. **Author contributions:** J.H., A.H., and A.V. conceived and designed the experiment, which was set up by L.A., J.H., and A.N. for the atom probe analysis and M.T., A.A., and J.H. for the terahertz generation and characterization. Experiments were carried out by J.H. and M.B., and the data were analyzed by A.V. and J.H. The detector system was designed and realized by G.D.C. The simulation was implemented by A.V. All authors discussed the results and contributed to the interpretation, and the manuscript was written by A.V. and A.H. **Competing interests:** The performances of the APT assisted by terahertz pulses are covered by the patent application number FR1908599. A.V., J.H., L.A., and A.H. are inventors on two pending patents related to this work filed by Centre National de la Recherche Scientifique (CNRS), Institut National des Sciences Appliquees de Rouen, and the Université de Rouen Normandie (no. FR1908599, filed 29 July 2019, and no. PCT/EP2020/070775, filed 23 July 2020). **Data and materials availability:** All data needed to evaluate the conclusions in the paper are present in the paper and/or the Supplementary Materials. Supplementary information is available in the online version of the paper. Correspondence and requests for materials should be addressed to A.V.

Submitted 8 July 2020
Accepted 23 December 2020
Published 10 February 2021
10.1126/sciadv.abd7259

Citation: A. Vella, J. Houard, L. Arnoldi, M. Tang, M. Boudant, A. Ayoub, A. Normand, G. Da Costa, A. Hideur, High-resolution terahertz-driven atom probe tomography. *Sci. Adv.* **7**, eabd7259 (2021).

Science Advances

High-resolution terahertz-driven atom probe tomography

Angela Vella, Jonathan Houard, Laurent Arnoldi, Mincheng Tang, Matthias Boudant, Anas Ayoub, Antoine Normand, Gerald Da Costa and Ammar Hideur

Sci Adv **7** (7), eabd7259.
DOI: 10.1126/sciadv.abd7259